

Visualized X-ray Dosimetry for Multienvironment Applications

Lan Lu, Songcheng Peng, Lei Zhao, Meiguang Zhang, Jianqiang Xiao, Hongyu Wen, Peng Zhang, Alexey Nikolaevich Yakovlev, Jianbei Qiu, Xue Yu, Ting Wang,* and Xuhui Xu*



Cite This: *Nano Lett.* 2023, 23, 8753–8760



Read Online

ACCESS |



Metrics & More



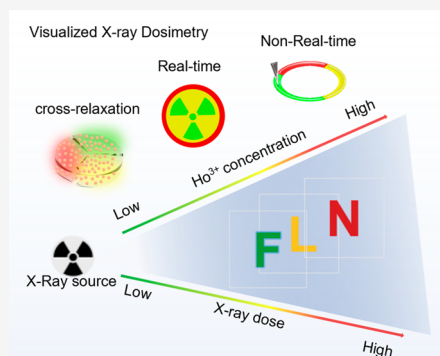
Article Recommendations



Supporting Information

ABSTRACT: X-ray dose detection plays a critical role in various scientific fields, including chemistry, materials, and medicine. However, the current materials used for this purpose face challenges in both immediate and delayed radiation detections. Here, we present a visual X-ray dosimetry method for multienvironment applications, utilizing NaLuF₄ nanocrystals (NCs) that undergo a color change from green to red upon X-ray irradiation. By adjustment of the concentrations of Ho³⁺, the emission color of the NCs can be tuned thanks to the cross-relaxation effects. Furthermore, X-ray irradiation induces generation of trapping centers in NaLuF₄:Ho³⁺ NCs, endowing the generation of mechanoluminescence (ML) behavior upon mechanical stimulation after X-ray irradiation ceases. The ML intensity shows a linear correlation with the X-ray dose, facilitating the detection of delayed radiation. This breakthrough facilitates X-ray dose inspection in flaw detection, nuclear medicine, customs, and civil protection, thereby enhancing opportunities for radiation monitoring and control.

KEYWORDS: X-ray dose detection, multienvironment, color-tunable, cross-relaxation



The detection of X-ray doses has become a crucial research area,^{1–5} given the wide range of applications for X-rays in industries such as nuclear industry,^{6,7} medical diagnosis,^{8,9} industrial material inspection,^{10,11} and security checks.^{12,13} Traditional X-ray dose detection methods rely on devices like thermoluminescent dosimeters,^{14–16} ionization chambers,^{17,18} and semiconductor detectors,^{19–21} which require complex readout instruments to convert X-ray energy into electrical signals.^{22–24} This approach has led to expensive, time-consuming, and unsuitable on-site real-time dose assessment.^{25,26} In contrast, photochromic materials capable of direct “visualization” under X-ray irradiation offer a direct and visual means of dose assessment, facilitating real-time evaluation of radiation exposure. Consequently, these intelligent visual materials hold considerable promise in the development of easy and portable systems for the elucidation of X-ray presence in visual inspection setups.^{27–29}

Well-developed X-ray-induced photochromic materials, such as BaMgSiO₄,³⁰ a viologen-based porous framework,³¹ Eu-MOF,³² and a dual-module photochromic nanocluster,³³ have been utilized for X-ray dose detection. However, these materials lack the capability to simultaneously accommodate real-time and delayed detection (the detection of prior radiation information following a cessation of X-ray excitation for a certain duration). To address this, trap-controlled mechanical luminescence (ML) materials have emerged as promising candidates for non-real-time X-ray dosimetry. These materials possess the capacity to store the energy of incident photons for a certain temporal duration, subsequently converting the mechanical energy to optical energy under

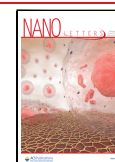
appropriate mechanical stimulation.^{34–38} Recently, Liu’s group reported the X-ray-induced generation of Frenkel defects in fluoride nanocrystals (NCs) (NaLuF₄:Tb³⁺) results in persistent performance, opening up new opportunities for X-ray delay detection.³⁹ The formation of anion Frenkel defects occurs through an elastic collision induced by high momentum photons, giving the fluoride NCs the ability to respond to mechanostimulation and X-ray stimulation. Besides, Peng et al. have recently designed effective trap centers in fluoride NCs that can respond to mechanostimulation, enabling three-dimensional non-real-time X-ray detection.⁴⁰ These studies manifest that the fluoride NCs offer new possibilities for simultaneous real-time and non-real-time X-ray dose detection.^{41,42} The combination of radio-luminescence (RL), X-ray-induced mechanoluminescence properties in fluoride NCs makes them a promising platform for visualization of X-ray dose detection in various environments.

Herein, we synthesize a series of NaLuF₄ NCs doped with different concentrations of the Ho³⁺ ion. These NCs exhibit excellent multicolor RL under X-ray irradiation, providing a simple real-time visual dosimeter for monitoring X-ray doses. In addition, NaLuF₄:Ho³⁺ NCs also manifest tunable

Received: July 28, 2023

Revised: September 13, 2023

Published: September 15, 2023



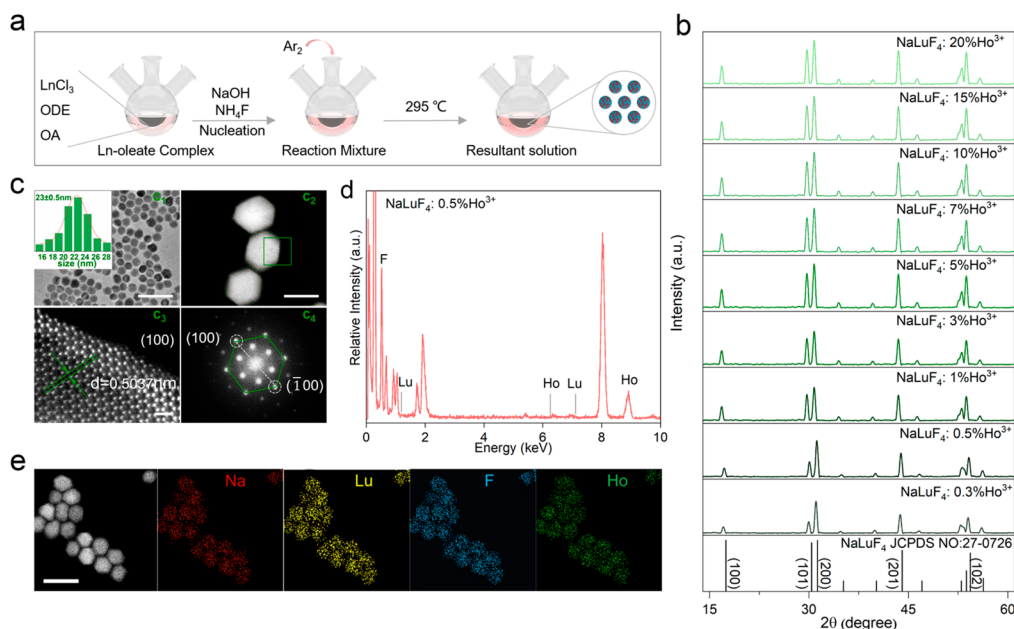


Figure 1. Phase structure characterization of the as-synthesized $\text{NaLuF}_4:\text{Ho}^{3+}$ NCs. (a) Schematic diagram of the synthesis process. (b) XRD patterns of $\text{NaLuF}_4:x\text{Ho}^{3+}$ ($x = 0.3\%$, 0.5% , 1% , 3% , 5% , 7% , 10% , 15% , and 20%) NCs. (c) TEM micrographs (scale bar 100 nm), (c_1) the corresponding size distribution (upper inset), (c_2) HAADF-STEM (scale bar 25 nm), (c_3) aberration-corrected HAADF-STEM (scale bar 2 nm), and (c_4) the corresponding FFT images of representative $\text{NaLuF}_4:0.5\% \text{Ho}^{3+}$ NCs. (d) XPS spectrum of $\text{NaLuF}_4:0.5\% \text{Ho}^{3+}$ NCs. (e) EDS mapping images of $\text{NaLuF}_4:0.5\% \text{Ho}^{3+}$ NCs (scale bar 50 nm).

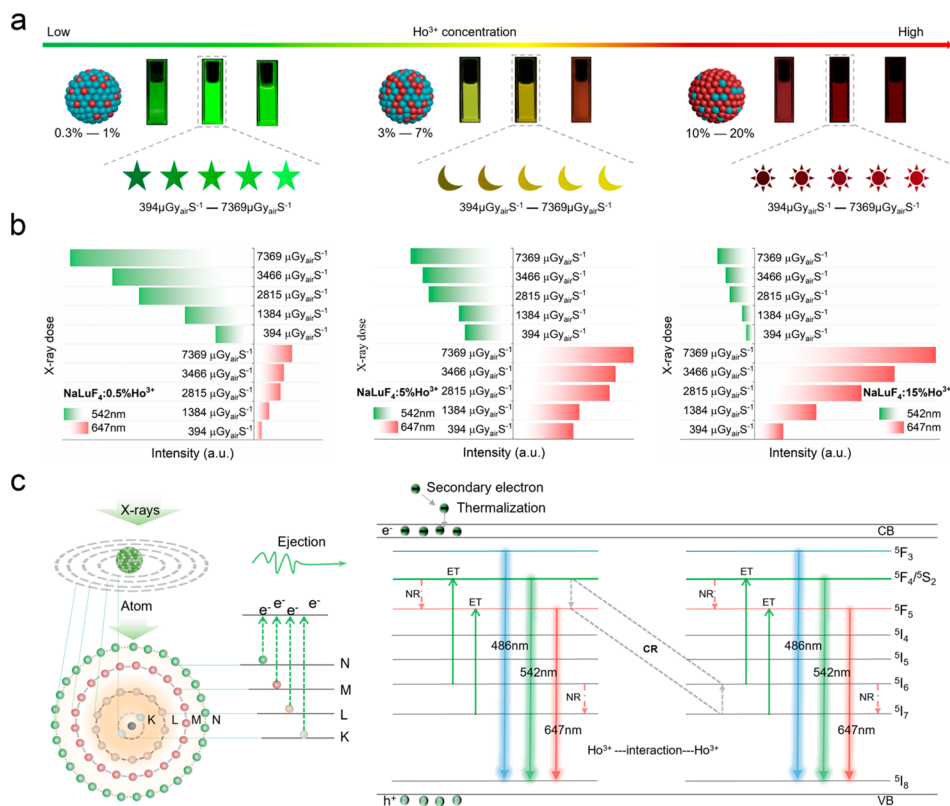


Figure 2. RL features of the $\text{NaLuF}_4:\text{Ho}^{3+}$ NCs. (a) Photographs of the $\text{NaLuF}_4:\text{Ho}^{3+}$ NCs doped with different concentrations of Ho^{3+} ions under varying X-ray irradiation doses. (b) RL intensities of $\text{NaLuF}_4:x\text{Ho}^{3+}$ ($x = 0.5\%$, 5% , and 15%) NCs by monitoring the wavelengths at 542 and 647 nm under varying X-ray irradiation doses. (c) RL mechanism of the $\text{NaLuF}_4:\text{Ho}^{3+}$ NCs.

mechanoluminescence upon mechanical stimulation, offering the capacity of delayed visual detection of X-ray doses. By understanding the underlying mechanisms responsible for

these properties, we gain insight into the behavior of the NCs and their application in X-ray dose detection. Moreover, by encompassing both real-time and delayed X-ray detections, our

method offers a versatile and comprehensive solution for radiation detection across different environments.

RESULTS AND DISCUSSION

A series of $\text{NaLuF}_4:x\text{Ho}^{3+}$ ($x = 0.3\%$, 0.5% , 1% , 3% , 5% , 7% , 10% , 15% , and 20%) NCs are synthesized via a hot-injection method (Figure 1a), and the corresponding X-ray diffraction (XRD) patterns are presented in Figure 1b. All diffraction peaks are consistent with the hexagonal-phase NaLuF_4 structure (JCPDS No. 27-0726) and no extra impurity phases emerge, indicating that the crystal structure of the NaLuF_4 NCs remains unchanged with the introduction of dopant Ho^{3+} ions. The cell volume of the NaLuF_4 NCs as a function of Ho^{3+} ion concentration is calculated (Figure S1), revealing the substitution of Ho^{3+} for Lu^{3+} in the host matrix. Transmission electron microscopy (TEM) and the corresponding histogram of the particle size distribution (Figure 1c₁) display the monodispersed hexagonal particles with average particle sizes of approximately 23 nm. The high-angle dark-field scanning transmission electron microscope (HAADF-STEM) image of the NCs in Figure 1c₂ confirms the well-defined and regular hexagonal morphology of the NaLuF_4 NCs. According to the enlarged HAADF-STEM image of Figure 1c₂, the lattice fringes could be well resolved and a d spacing of 0.5037 nm can be observed, which is attributed to the (100) plane of the NaLuF_4 phase (Figure 1c₃). The selected area fast Fourier transformation (FFT) based on the HAADF-STEM image is presented in Figure 1c₄, which displays the characteristic shape of the hexagonal NaLuF_4 phase. These results further demonstrate the successful formation of the $\text{NaLuF}_4:\text{Ho}^{3+}$ NCs with high crystallinity. The XPS spectrum of the samples clearly detects the peaks, corresponding to Na(1s), F(1s), C(1s), Lu(4d), Lu(4f), and Ho(4d), respectively (Figure 1d) in $\text{NaLuF}_4:0.5\% \text{Ho}^{3+}$ NCs. Furthermore, the TEM morphology, the corresponding mapping images (Figure 1e), and energy dispersive X-ray spectroscopy (EDS) (Figure S2) show that Na, Lu, F, and Ho ions are homogeneously dispersed within the as-obtained $\text{NaLuF}_4:\text{Ho}^{3+}$ NCs.

Here, the RL spectra of the as-synthesized NCs are measured under X-ray operation with a voltage of 40 kV and a tube current of 30 mA (Figure S3). The obtained RL spectra display three distinct narrow intense emission bands, which derive from the transitions $^5\text{F}_3 \rightarrow ^5\text{I}_8$ (486 nm), $^5\text{F}_4/^5\text{S}_2 \rightarrow ^5\text{I}_8$ (542 nm), and $^5\text{F}_5 \rightarrow ^5\text{I}_8$ (647 nm) of Ho^{3+} ions. Additionally, the RL intensity of these samples gradually increases with an increase in the Ho^{3+} concentration and achieves the maximum intensity when $x = 0.5\%$ thanks to the concentration quenching⁴³ (Figure S4). It is fascinating to note that the $\text{NaLuF}_4:\text{Ho}^{3+}$ NCs exhibit tunable RL colors, ranging from green to red, by varying the concentration of Ho^{3+} ions (ranging from 0.03 to 20 mol %), as given in Figure 2a and Figure S5. This indicates that the RL color of the NCs can be adjusted by manipulating the concentration of the Ho^{3+} ions. The observed color transition in the $\text{NaLuF}_4:\text{Ho}^{3+}$ NCs is indeed expected to be primarily attributed to the combined effect of a cross-relaxation process (CR) between the different concentrations of doped Ho^{3+} ions.⁴⁴ Additionally, the emitted RL intensity gradually increases as the X-ray dose increases from 394 to 7369 $\mu\text{Gy}_{\text{air}} \text{S}^{-1}$, suggesting that the RL emission of the NCs is directly influenced by the intensity of the X-ray dose. RL intensity is demonstrated to be linearly correlated with the X-ray dose rate as plotted in Figure S6, and the detection limit is determined to be 48.537 $\mu\text{Gy}_{\text{air}} \text{S}^{-1}$. In

addition, a stability test on $\text{NaLuF}_4:0.5\% \text{Ho}^{3+}$ NCs under X-ray irradiation confirms that the NCs exhibit excellent stability when exposed to X-ray irradiation (Figure S7). Additionally, to achieve visualized X-ray dose detection, we carefully selected three representative samples, $\text{NaLuF}_4:x\text{Ho}^{3+}$ ($x = 0.5\%$, 5% , and 15%) NCs, with contrasting colors and luminescence intensities, and the corresponding RL intensities were measured by monitoring the wavelength at 542 and 647 nm under various doses of X-rays, as depicted in Figure 2b. It is observed that the emission intensity gradually increased with the increases of the X-ray radiation dose, which is due to more carriers being filled at the $^5\text{F}_4$ and $^5\text{F}_5$ energy levels with the increases of the X-ray radiation dose. Additionally, the red–green ratio of the three samples at different cycle counts is also investigated (Figures S8–S10), and the results demonstrate a high level of stability of the as-obtained NCs. It is worth noting that the $\text{NaLuF}_4:0.5\% \text{Ho}^{3+}$ NCs display green UC emission when irradiated with a 980 nm laser but do not exhibit luminescence under solar and ultraviolet irradiation. This can be attributed to the relatively large band gap of NaLuF_4 , which is 7.2591 eV (Figure S11). Neither sunlight nor UV light possess enough energy to excite electrons from the valence band to the conduction band, resulting in the absence of luminescence. Notably, a series of $\text{NaLuF}_4:1\% \text{Yb}^{3+}, x\text{Ho}^{3+}$ ($x = 0.3\%$, 0.5% , 1% , 3% , 5% , 7% , 10% , 15% , and 20%) NCs also exhibit color-tuning properties under 980 nm laser irradiation based on a two-photon absorption process (Figure S12). The large numbers of sufficient 4f energy levels in Ho^{3+} ions facilitate energy adaptation transfer between different energy levels, enabling the CR effect between adjacent Ho^{3+} ions to be easier. With an increase in Ho^{3+} concentration, the fluorescence decay lifetime of the $^5\text{F}_4/^5\text{S}_2$ level decreased significantly, while the fluorescence decay lifetime of the $^5\text{F}_5$ level was enhanced. This can be attributed to the faster reduction of Ho^{3+} ions at the $^5\text{F}_4/^5\text{S}_2$ level and their population at the $^5\text{F}_5$ energy level caused by the CR process: $[(^5\text{F}_4, ^5\text{S}_2), ^5\text{I}_7] \rightarrow [^5\text{F}_5, ^5\text{I}_6]$ (Figure S13). Thus, the multicolor mechanism of the X-ray-induced photochromic properties in the NCs can also be attributed to the CR effect between doped Ho^{3+} ions of different concentrations.

Accordingly, the mechanism of the tunable RL color of the $\text{NaLuF}_4:\text{Ho}^{3+}$ NCs are proposed as shown in Figure 2c. When the $\text{NaLuF}_4:\text{Ho}^{3+}$ NCs are exposed to X-ray radiation, the incident X-ray photons interact with the atoms in the NCs and then result in a photoelectric effect. Subsequently, X-ray photons can transfer sufficient energy to the valence electrons of the atoms, causing them to be ejected from the atom, thereby creating electron–hole pairs. These electron–hole pairs are then transported to Ho^{3+} luminescence centers and then captured by energy traps, such as E-trap and H-trap. These energy traps are probably fluoride anion Frenkel defects formed during the X-ray irradiation as previously reported.³⁹ Once the excited levels of lanthanide activators are populated via the absorption of energy from the recombination of the low kinetic energy carriers, X-ray-excited optical luminescence (XEOL) is generated. As the concentration of doped Ho^{3+} ions increases, the distance between neighboring Ho^{3+} ions becomes shorter, facilitating the CR process $[(^5\text{F}_4, ^5\text{S}_2), ^5\text{I}_7] \rightarrow [^5\text{F}_5, ^5\text{I}_6]$. Consequently, this leads to an enhancement of the red emission band and a weakening of the green emission band, thereby resulting in the observed color-tuning RL phenomenon.

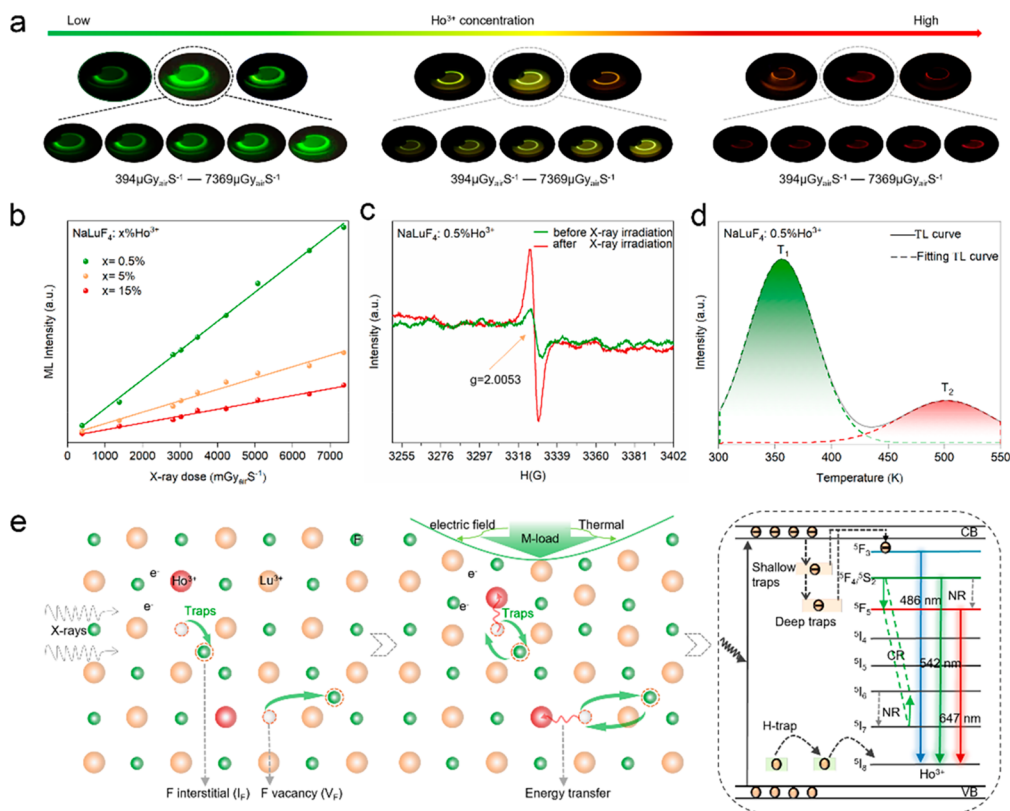


Figure 3. ML feature of the $\text{NaLuF}_4:\text{Ho}^{3+}$ NCs after being charged by an X-ray source. (a) ML photographs of $\text{NaLuF}_4:x\text{Ho}^{3+}$ ($x = 0.3\%$, 0.5% , 1% , 3% , 5% , 7% , 10% , 15% , and 20%) NCs after being charged by different X-ray doses. The upload force was 10 N. (b) Linear dependence of the ML integrated intensity of $\text{NaLuF}_4:x\text{Ho}^{3+}$ ($x = 0.5\%$, 5% , and 15%) NCs as a function of X-ray dose. (c) EPR spectra of $\text{NaLuF}_4:\text{Ho}^{3+}$ NCs before and after X-ray irradiation. (d) TL curves of $\text{NaLuF}_4:0.5\% \text{Ho}^{3+}$ NCs after being charged by X-ray for 5 min. (e) ML mechanism of the $\text{NaLuF}_4:\text{Ho}^{3+}$ NCs.

Furthermore, it is noted that the composited films of the $\text{NaLuF}_4:x\text{Ho}^{3+}$ ($x = 0.3\%$, 0.5% , 1% , 3% , 5% , 7% , 10% , 15% , and 20%) NCs, encapsulated within epoxy resin (ER), exhibit bright multicolored ML behavior after being charged with distinct X-ray doses (ranging from 394 to 7369 $\mu\text{Gy}_{\text{air}} \text{S}^{-1}$) by the friction-illuminated machine (Figure S14), as given in Figure 3a and Videos S1–S3. The ML behavior of the $\text{NaLuF}_4:\text{Ho}^{3+}@ER$ composited film was found to be identical to the RL characteristics of the sample (Figure S15). Additionally, the ML intensity of $\text{NaLuF}_4:x\text{Ho}^{3+}@ER$ ($x = 0.5\%$, 5% , and 15%) composited film gradually increased with increasing X-ray radiation dose, as depicted in Figure 3b and Figure S16. This can be attributed to the filling of more carriers in traps as the X-ray radiation dose increases. Subsequently, these carriers are released to produce ML emission upon mechanical stimulation and then result in the enhancement of the ML intensity. The linear relationship between the ML intensity and X-ray dose allows for accurate measurement of the dose based on observed changes in ML intensity. Additionally, Figure S17 showcases the ML intensity as a function of loaded force, which reveals that the ML detection limit of NCs is determined to be 0.2131 N. It is expected that the ML performance results from the formation of defects after X-ray irradiation. Therefore, to investigate the detailed mechanism of the ML features, the EPR signals of the $\text{NaLuF}_4:0.5\% \text{Ho}^{3+}$ NCs sample before and after X-ray irradiation are measured (Figure 3c). It can be observed that the EPR signal of the sample is significantly enhanced after X-ray irradiation ($g = 2.0053$), where g represents the scaling

factor considering the coupling between orbital and spin angular momentum. These results confirm that it is possible to induce high-density trap states in $\text{NaLuF}_4:0.5\% \text{Ho}^{3+}$ NCs using high-momentum X-ray photons, as previously reported.³⁹ These trap states are potentially responsible for the multicolored ML behavior exhibited by the NCs. To further investigate the formation of the defects induced by X-ray irradiation, the thermoluminescence curves (TL) curves of a series of $\text{NaLuF}_4:\text{Ho}^{3+}$ NCs are measured (Figure S18a). The Gaussian fitted TL curves of the representative sample are given in Figure 3d, which contains two broad bands, ascribed to shallow trap T_1 (355 K) and deep trap T_2 (502 K). The corresponding trap depths are calculated to be 0.712 and 1.004 eV, respectively. After the X-ray radiation ceases, no visible afterglow is observed by the naked eye. However, under external loaded stress, bright ML behavior occurs. This indicates that the stress can induce the release of the carriers from the deep traps, thereby contributing to the ML behavior.

The band gap of the sample was examined under different applied loads, revealing an unchanged band gap within the range of applied loads (Figure S19). Hence, we summarize the ML mechanism of the samples as follows (Figure 3e). The high energy of X-rays is primarily absorbed by the lutetium atoms, which have a high X-ray absorption coefficient (4.03 cm/g). The ground-state electrons become high-energy electrons and then transition to the excited state due to the energy transition. Subsequently, large numbers of fluoride vacancies are created concurrent with the generation of fluoride interstitial ions. This leads to the formation of trap

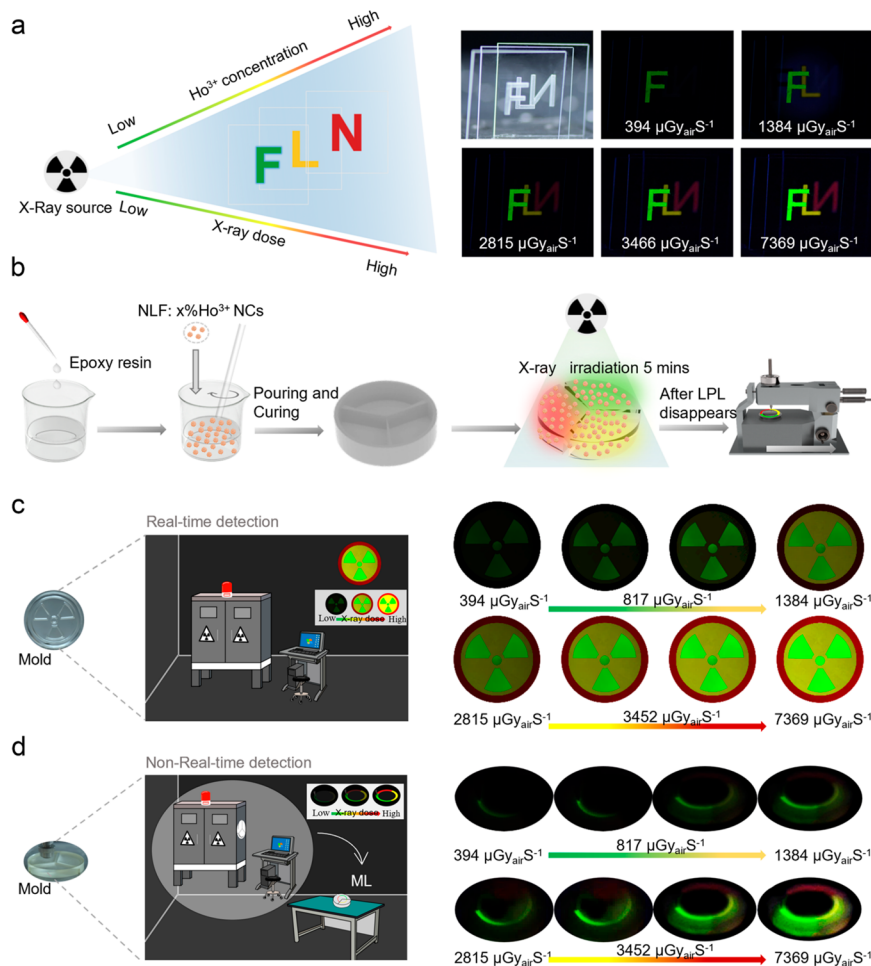


Figure 4. Applications of NaLuF₄:Ho³⁺ NCs in X-ray dose detection. Schematic diagram and photographs of (a) tricolor laminated devices and (b) tricolor warning mold for real-time visualization of X-ray dose detection. (c) Schematic diagram of tricolor ML mold fabrication process. (d) Schematic diagram and photographs of the as-obtained tricolor mold for non-real-time visualization of X-ray dose detection.

pairs in an unstable state, the same as previously reported.³⁹ Once the carriers in the shallow traps are nearly all released at room temperature, the carrier trapped in the deep traps is released when friction is applied on the film. Thereafter, the excited carrier is converted to a hot carrier with high energy that is accelerated toward the luminescent center of Ho³⁺ ions. This migration process generates a transient ML. When the concentration of doped Ho³⁺ ions increases, the CR process [(⁵F₄, ⁵S₂), (⁵I₇)] → [(⁵F₅, ⁵I₆)] between neighboring Ho³⁺ ions becomes more prevalent and then leads to the manifestation of multicolored ML behavior. Additionally, the unique ML properties of the NaLuF₄:Ho³⁺@ER film were found to be partly attributable to the triboelectricity-induced EL model, as evidenced by the changes in electric potential and electroluminescence of the NaLuF₄:Ho³⁺ NCs (Figures S20–S22).

The presence of color-tunable emissions and carrier storage in NaLuF₄ NCs makes them suitable for visual dose detection of X-rays, in both real-time and non-real-time scenarios. By choosing samples with contrasting colors and different sensitivities to X-ray radiation, we are able to demonstrate a clear distinction in the color response at different X-ray doses. As depicted in Figure 4a, we etched three different letters “F”, “L”, and “N” onto a quartz wafer and incorporated three samples, NaLuF₄:xHo³⁺ ($x = 0.5\%$, 5% , and 15%) NCs, which exhibit contrasting colors. Due to the cross-relaxation and concentration quenching phenomena between Ho³⁺ ions of

different concentrations, under the same dose of X-ray irradiation, the letters on the three quartz sheets change from green to red, and the luminous intensity is gradually increased with the dose of X-ray increasing from 394 to 7369 μGy_{air} S⁻¹. The observed relationship between the X-ray dose and the corresponding increase in the luminous intensity indicates that the response of the luminescent material to X-rays is stable and predictable. By visualizing the color change, it becomes possible to estimate or monitor the X-ray dose in real time without the need for complex instrumentation. As shown in Figure 4b, we make the three colors of the film into a “flat warning mold” based on the above three samples. The intensity of the NaLuF₄:Ho³⁺ film gradually increases with an increase of the X-ray radiation and more visual observation of color and intensity changes on a “flat warning mold”. The ability of the warning mold to visually identify the X-ray dose with the naked eye is highly beneficial for real-time visualization of X-ray dose detection. This provides a quick and convenient method for determining the radiation exposure levels. In addition, the creation of a three-color “ML detect mold”, encapsulated in biocompatible polymer epoxy resin, further expands the application possibilities (Figure 4c). Under an external force stimulation, the captured carriers within the deep traps of the material are released. Similar to the previous observation, the ML emission of the “ML detect mold” changes from green to red, and the ML intensity increases with

increasing X-ray radiation (Figure 4d), indicating that this irradiated mold can be used for non-real-time visualization of X-ray dose detection. This allows the experimental staff to infer the time of entry into the radiation environment and avoid exposure to excess dose radiation. Overall, the combination of real-time and non-real-time visualization capabilities makes the $\text{NaLuF}_4:\text{Ho}^{3+}$ materials highly practical and useful for monitoring and assessing radiation exposure levels, ensuring the safety of experimental staff in radiation environments.

CONCLUSION

In summary, the potential of $\text{NaLuF}_4:\text{Ho}^{3+}$ NCs as versatile dosimeters for X-ray radiation has been demonstrated. A reversible color change from green to red at 394 to 7369 $\mu\text{Gy}_{\text{air}}$ S^{-1} doses of X-ray irradiation was observed, allowing for real-time dosimetry. Moreover, the multicolored ML behavior of the $\text{NaLuF}_4:\text{Ho}^{3+}$ NCs composited film remains even after the removal of X-ray irradiation, making it suitable for non-real-time detection. The ML behavior is believed to be caused by a combination of thermoluminescence and electroluminescence generated by friction. Visible color changes can be observed with the naked eye, allowing for qualitative detection of X-ray doses, while quantitative detection can be accomplished through the linear relationship between X-ray doses and luminescence intensity. This innovative approach simplifies the complex process of X-ray dose detection and opens up possibilities for a wide range of application environments. The $\text{NaLuF}_4:\text{Ho}^{3+}$ NCs hold great potential as a smart material for X-ray exposure detection, with broad prospects in scientific research and rapid nondestructive testing.

ASSOCIATED CONTENT

Supporting Information

The Supporting Information is available free of charge at <https://pubs.acs.org/doi/10.1021/acs.nanolett.3c02826>.

ML behavior of 0.5% Ho^{3+} NCs@ER film (MP4)

Materials fabrications, EDS, RL spectra, PL spectra of NCs under 980 nm laser, lifetime curves, calculations of cross-relaxation rate, TL fitting curve, ML photographs and spectra of NCs under different forces, CL spectrum, electric potential spectra, the electronic band structures calculations of NaLuF_4 (PDF)

ML behavior of 5% Ho^{3+} NCs@ER film (MP4)

ML behavior of 15% Ho^{3+} NCs@ER film (MP4)

AUTHOR INFORMATION

Corresponding Authors

Xuhui Xu – Faculty of Materials Science and Engineering, Kunming University of Science and Technology, Kunming 650093 Yunnan, People's Republic of China; orcid.org/0000-0002-0721-7304; Email: xuxuh07@126.com

Ting Wang – School of Materials and Chemistry and Chemical Engineering, Chengdu University of Technology, Chengdu 610059 Sichuan, People's Republic of China; orcid.org/0000-0002-7549-3888; Email: wangtkm@foxmail.com

Authors

Lan Lu – Faculty of Materials Science and Engineering, Kunming University of Science and Technology, Kunming 650093 Yunnan, People's Republic of China

Songcheng Peng – Faculty of Materials Science and Engineering, Kunming University of Science and Technology, Kunming 650093 Yunnan, People's Republic of China

Lei Zhao – College of Physics and Optoelectronic Technology, Collaborative Innovation Center of Rare-Earth Functional Materials and Devices Development, Baoji University of Arts and Sciences, Baoji 721016, People's Republic of China; orcid.org/0000-0002-5811-0793

Meiguang Zhang – College of Physics and Optoelectronic Technology, Collaborative Innovation Center of Rare-Earth Functional Materials and Devices Development, Baoji University of Arts and Sciences, Baoji 721016, People's Republic of China; orcid.org/0000-0001-7219-843X

Jianqiang Xiao – Faculty of Materials Science and Engineering, Kunming University of Science and Technology, Kunming 650093 Yunnan, People's Republic of China

Hongyu Wen – Faculty of Materials Science and Engineering, Kunming University of Science and Technology, Kunming 650093 Yunnan, People's Republic of China

Peng Zhang – Faculty of Materials Science and Engineering, Kunming University of Science and Technology, Kunming 650093 Yunnan, People's Republic of China; orcid.org/0000-0002-9214-2983

Alexey Nikolaevich Yakovlev – T.F. Gorbachev Kuzbass State Technical University, Kemerovo 650000, Russia

Jianbei Qiu – Faculty of Materials Science and Engineering, Kunming University of Science and Technology, Kunming 650093 Yunnan, People's Republic of China; orcid.org/0000-0002-3699-3310

Xue Yu – School of Mechanical Engineering, Institute for Advanced Materials Deformation and Damage from Multi-Scale, Chengdu University, Chengdu 610106, People's Republic of China; orcid.org/0000-0002-9025-2556

Complete contact information is available at: <https://pubs.acs.org/doi/10.1021/acs.nanolett.3c02826>

Author Contributions

L.L. and X.X. conceived the experiments. S.P., J.X., H.W., P.Z., and A.N.Y. were responsible for assisting with experiments. L.L. was primarily responsible for the experiments. L.Z. and M.Z. were responsible for electronic band structure calculations. X.Y. and T.W. were responsible for checking and revising the first draft. J.Q. gave suggestions of conceptual ideas for the manuscript. All authors contributed to the data analyses.

Notes

The authors declare no competing financial interest.

ACKNOWLEDGMENTS

This work was financially supported by the Science and Technology Talents and Platform Program (Workstation for academicians and Experts) (202205AF150005), the Yunnan Major Scientific and Technological Projects (grant no. 202202AG050004), the Sichuan Natural Science Foundation (2022YFH0108, 2022JDJQ0030), the National Nature Science Foundation of China (NSFC) (U2241236, 1220041913), and the Young Elite Scientists Sponsorship Program by CAST (2022QNR001).

REFERENCES

- Yukihara, E. G.; McKeever, S. W. S.; Andersen, C. E.; Bos, A. J. J.; Bailiff, I. K.; Yoshimura, E. M.; Sawakuchi, G. O.; Bossin, L.;

- Christensen, J. B. Luminescence dosimetry. *Nature Reviews Methods Primers* **2022**, *2* (1), 26.
- (2) Wang, Z.; Wang, Y.; Ge, Z.; Tian, Y.; Ai, M.; Cao, S.; Wang, M.; Wang, S.; Ma, J. Color-phase readout radiochromic photonic crystal dosimeter. *Matter* **2022**, *5* (11), 4060–4075.
- (3) Lyu, Q.; Neph, R.; Sheng, K. Tomographic detection of photon pairs produced from high-energy X-rays for the monitoring of radiotherapy dosing. *Nat. Biomed Eng.* **2023**, *7* (3), 323–334.
- (4) Yang, Z.; Hu, J.; Van der Heggen, D.; Feng, A.; Hu, H.; Vrielinck, H.; Smet, P. F.; Poelman, D. Realizing Simultaneous X-Ray Imaging and Dosimetry Using Phosphor-Based Detectors with High Memory Stability and Convenient Readout Process. *Adv. Funct. Mater.* **2022**, *32* (31), No. 2201684.
- (5) Aboelezz, E.; Pogue, B. W. Review of nanomaterial advances for ionizing radiation dosimetry. *Appl. Phys. Rev.* **2023**, *10* (2), No. 021312.
- (6) Du, M.; Wang, J.; Xu, S.; Li, H.; Zhang, Z.; Qi, Y.; Lv, S.; Qiu, J.; Yan, Y.; Zhou, S. Super-elastic Scintillating Fibers and Fabrics for Efficient and Visual Radiation Detection. *Advanced Fiber Materials* **2023**, *5* (4), 1493–1504.
- (7) Ding, H.; Dixon Wilkins, M. C.; Gausse, C.; Mottram, L. M.; Sun, S.; Stennett, M. C.; Grolimund, D.; Tappero, R.; Nicholas, S.; Hyatt, N. C.; Corkhill, C. L. Safely probing the chemistry of Chernobyl nuclear fuel using micro-focus X-ray analysis. *Journal of Materials Chemistry A* **2021**, *9* (21), 12612–12622.
- (8) Luo, Z.; Wu, Y.; Wang, Y.; Hu, D.; Gao, D.; Ge, Y.; Sheng, Z.; Liu, X.; Zheng, H. Clinical radiation dose verification by topographic persistent luminescence dosimetry. *Nano Today* **2023**, *50*, No. 101854.
- (9) Hou, B.; Yi, L.; Hu, D.; Luo, Z.; Gao, D.; Li, C.; Xing, B.; Wang, J. W.; Lee, C. N.; Zhang, R.; Sheng, Z.; Zhou, B.; Liu, X. A swallowable X-ray dosimeter for the real-time monitoring of radiotherapy. *Nat. Biomed Eng.* **2023**, DOI: 10.1038/s41551-023-01024-2.
- (10) Cao, C.; Toney, M. F.; Sham, T.-K.; Harder, R.; Shearing, P. R.; Xiao, X.; Wang, J. Emerging X-ray imaging technologies for energy materials. *Mater. Today* **2020**, *34*, 132–147.
- (11) Hemonnot, C. Y. J.; Koster, S. Imaging of Biological Materials and Cells by X-ray Scattering and Diffraction. *ACS Nano* **2017**, *11* (9), 8542–8559.
- (12) Han, J. S.; Lee, S. H.; Go, H.; Kim, S. J.; Noh, J. H.; Lee, C. J. High-Performance Cold Cathode X-ray Tubes Using a Carbon Nanotube Field Electron Emitter. *ACS Nano* **2022**, *16* (7), 10231–10241.
- (13) Gupta, P.; Sinno, Z.; Glover, J. L.; Paulter, N. G.; Bovik, A. C. Predicting Detection Performance on Security X-Ray Images as a Function of Image Quality. *IEEE Trans Image Process* **2019**, *28* (7), 3328–3342.
- (14) Sinclair, S. A.; Pech-Canul, M. I. Development feasibility of TLD phosphors and thermoluminescent composite materials for potential applications in dosimetry: A review. *Chemical Engineering Journal* **2022**, *443*, No. 136522.
- (15) Hsu, K. C. TCTAP A-062 An Easy Method to Evaluate Radiation Peak Skin Dose in the Coronary Angiography by Using a Simulating Phantom and Thermoluminescent Dosimeters. *Journal of the American College of Cardiology* **2022**, *79* (15), S38.
- (16) Klepa, R. B.; Medeiros, M. F.; Franco, M. A. C.; Tamberg, E. T.; Farias, T. M. d. B.; Paschoalin Filho, J. A.; Berssaneti, F. T.; Santana, J. C. C. Reuse of construction waste to produce thermoluminescent sensor for use in highway traffic control. *Journal of Cleaner Production* **2019**, *209*, 250–258.
- (17) Vahabi, S. M.; Shamsaei Zafarghandi, M. Investigations of radiation properties, photon interaction parameters and water equivalence of some polymers used in the construction of ionization chambers for low energy X-ray beams. *Measurement* **2020**, *151*, No. 107210.
- (18) Colette, D.; Mazon, D.; Barnsley, R.; O'Mullane, M.; Jardin, A.; Sirinelli, A. Conceptual study of energy resolved x-ray measurement and electron temperature reconstruction on ITER with low voltage ionization chambers. *Rev. Sci. Instrum.* **2021**, *92* (8), No. 083511.
- (19) Pan, L.; Liu, Z.; Welton, C.; Klepov, I.; Peters, J. A.; De Siena, M. C.; Benadia, A.; Pandey, I.; Miceli, A.; Chung, D. Y.; Reddy, G. N. M.; Wessels, B. W.; Kanatzidis, M. G. Ultrahigh-Flux X-ray Detection by a Solution-Grown Perovskite CsPbBr₃ Single-Crystal Semiconductor Detector. *Adv. Mater.* **2023**, *35* (25), No. e2211840.
- (20) Nanayakkara, M. P. A.; Masteghin, M. G.; Basirico, L.; Fratelli, I.; Ciavatti, A.; Kilbride, R. C.; Jenatsch, S.; Webb, T.; Richheimer, F.; Wood, S.; Castro, F. A.; Parnell, A. J.; Fraboni, B.; Jayawardena, K.; Silva, S. R. P. Molecular Weight Tuning of Organic Semiconductors for Curved Organic-Inorganic Hybrid X-Ray Detectors. *Adv. Sci. (Weinh)* **2022**, *9* (2), No. e2101746.
- (21) Wu, S.; Liang, C.; Zhang, J.; Wu, Z.; Wang, X. L.; Zhou, R.; Wang, Y.; Wang, S.; Li, D. S.; Wu, T. A Photoconductive X-ray Detector with a High Figure of Merit Based on an Open-Framework Chalcogenide Semiconductor. *Angew. Chem., Int. Ed. Engl.* **2020**, *59* (42), 18605–18610.
- (22) Yakunin, S.; Sytnyk, M.; Kriegner, D.; Shrestha, S.; Richter, M.; Matt, G. J.; Azimi, H.; Brabec, C. J.; Stangl, J.; Kovalenko, M. V.; Heiss, W. Detection of X-ray photons by solution-processed organic-inorganic perovskites. *Nat. Photonics* **2015**, *9* (7), 444–449.
- (23) Wu, H.; Ge, Y.; Niu, G.; Tang, J. Metal Halide Perovskites for X-Ray Detection and Imaging. *Matter* **2021**, *4* (1), 144–163.
- (24) Daum, M.; Deumel, S.; Sytnyk, M.; Afify, H. A.; Hock, R.; Eigen, A.; Zhao, B.; Halik, M.; These, A.; Matt, G. J.; Brabec, C. J.; Tedde, S. F.; Heiss, W. Self-Healing Cs₃Bi₂Br₃l₆ Perovskite Wafers for X-Ray Detection. *Advanced Functional Materials* **2021**, *31* (47), 2102713.
- (25) Liu, L.; Li, W.; Feng, X.; Guo, C.; Zhang, H.; Wei, H.; Yang, B. Energy Transfer Assisted Fast X-ray Detection in Direct/Indirect Hybrid Perovskite Wafer. *Adv. Sci. (Weinh)* **2022**, *9* (15), No. e2103735.
- (26) Ma, C.; Li, H.; Chen, M.; Liu, Y.; Zhao, K.; Liu, S. Water-Resistant Lead-Free Perovskitoid Single Crystal for Efficient X-Ray Detection. *Adv. Funct. Mater.* **2022**, *32* (30), No. 2202160.
- (27) Vuori, S.; Colinet, P.; Norrbo, I.; Steininger, R.; Saarinen, T.; Palonen, H.; Paturi, P.; Rodrigues, L. C. V.; Göttlicher, J.; Le Bahers, T.; Lastusaari, M. Detection of X-Ray Doses with Color-Changing Hackmanites: Mechanism and Application. *Advanced Optical Materials* **2021**, *9* (20), No. 2100762.
- (28) Wang, M. S.; Yang, C.; Wang, G. E.; Xu, G.; Lv, X. Y.; Xu, Z. N.; Lin, R. G.; Cai, L. Z.; Guo, G. C. A room-temperature X-ray-induced photochromic material for X-ray detection. *Angew. Chem., Int. Ed. Engl.* **2012**, *51* (14), 3432–5.
- (29) Zhao, W.; Wang, Y.; Guo, Y.; Suh, Y. D.; Liu, X. Color-Tunable and Stable Copper Iodide Cluster Scintillators for Efficient X-Ray Imaging. *Adv. Sci. (Weinh)* **2023**, *10* (5), No. e2205526.
- (30) Yang, Z.; Hu, J.; Van der Heggen, D.; Jiao, M.; Feng, A.; Vrielinck, H.; Smet, P. F.; Poelman, D. A Versatile Photochromic Dosimeter Enabling Detection of X-Ray, Ultraviolet, and Visible Photons. *Laser & Photonics Reviews* **2023**, *17* (5), 2200809.
- (31) Chen, C.; Sun, J. K.; Zhang, Y. J.; Yang, X. D.; Zhang, J. Flexible Viologen-Based Porous Framework Showing X-ray Induced Photochromism with Single-Crystal-to-Single-Crystal Transformation. *Angew. Chem., Int. Ed. Engl.* **2017**, *56* (46), 14458–14462.
- (32) Sun, Y. H.; Li, C. L.; Wang, W. F.; Wang, S. H.; Li, P. X.; Guo, G. C. A photochromic and scintillation Eu-MOF with visual X-ray detection in bright and dark environments. *Chem. Commun. (Camb)* **2022**, *58* (25), 4056–4059.
- (33) Lu, H.; Xie, J.; Wang, X. Y.; Wang, Y.; Li, Z. J.; Diefenbach, K.; Pan, Q. J.; Qian, Y.; Wang, J. Q.; Wang, S.; Lin, J. Visible colorimetric dosimetry of UV and ionizing radiations by a dual-module photochromic nanocluster. *Nat. Commun.* **2021**, *12* (1), No. 2798.
- (34) Matsui, H.; Xu, C.-N.; Tateyama, H. Stress-stimulated luminescence from ZnAl₂O₄:Mn. *Appl. Phys. Lett.* **2001**, *78* (8), 1068–1070.
- (35) Zhang, J.-C.; Wang, X.; Marriott, G.; Xu, C.-N. Trap-controlled mechanoluminescent materials. *Prog. Mater. Sci.* **2019**, *103*, 678–742.

- (36) Wang, Z. L.; Wang, A. C. On the origin of contact-electrification. *Mater. Today* **2019**, *30*, 34–51.
- (37) Zhuang, Y.; Xie, R. J. Mechanoluminescence Rebrightening the Prospects of Stress Sensing: A Review. *Adv. Mater.* **2021**, *33* (50), No. e2005925.
- (38) Guo, X.; Bian, J.; Bai, Y.; Ma, Z.; Yang, S.; Wang, Z. Trap-independent mechanoluminescence in $\text{ZnB}_2\text{O}_4:\text{Mn}^{2+}$ /PDMS composite elastomer with self-recovery activity. *Chem. Phys. Lett.* **2022**, *787*, No. 139235.
- (39) Ou, X.; Qin, X.; Huang, B.; Zan, J.; Wu, Q.; Hong, Z.; Xie, L.; Bian, H.; Yi, Z.; Chen, X.; Wu, Y.; Song, X.; Li, J.; Chen, Q.; Yang, H.; Liu, X. High-resolution X-ray luminescence extension imaging. *Nature* **2021**, *590* (7846), 410–415.
- (40) Peng, S.; Xia, P.; Wang, T.; Lu, L.; Zhang, P.; Zhou, M.; Zhao, F.; Hu, S.; Kim, J. T.; Qiu, J.; Wang, Q.; Yu, X.; Xu, X. Mechanoluminescence Behavior of Lanthanide-Doped Fluoride Nanocrystals for Three-Dimensional Stress Imaging. *ACS Nano* **2023**, *17* (10), 9543–9551.
- (41) Pei, P.; Chen, Y.; Sun, C.; Fan, Y.; Yang, Y.; Liu, X.; Lu, L.; Zhao, M.; Zhang, H.; Zhao, D.; Liu, X.; Zhang, F. X-ray-activated persistent luminescence nanomaterials for NIR-II imaging. *Nat. Nanotechnol.* **2021**, *16* (9), 1011–1018.
- (42) Zhuang, Y.; Chen, D.; Chen, W.; Zhang, W.; Su, X.; Deng, R.; An, Z.; Chen, H.; Xie, R.-J. X-ray-charged bright persistent luminescence in $\text{NaYF}_4:\text{Ln}^{3+}@\text{NaYF}_4$ nanoparticles for multidimensional optical information storage. *Light: Science & Applications* **2021**, *10* (1), 132.
- (43) Chen, B.; Wang, F. Combating Concentration Quenching in Upconversion Nanoparticles. *Acc. Chem. Res.* **2020**, *53* (2), 358–367.
- (44) Zhou, J.; Deng, J.; Zhu, H.; Chen, X.; Teng, Y.; Jia, H.; Xu, S.; Qiu, J. Up-conversion luminescence in $\text{LaF}_3:\text{Ho}^{3+}$ via two-wavelength excitation for use in solar cells. *Journal of Materials Chemistry C* **2013**, *1* (48), 8023–8027.